



Universiteit
Leiden
The Netherlands

Multi-epoch properties of the warm absorber in the Seyfert 1 galaxy NGC 985

Ebrero, J.; Domček, V.; Kriss, G.A.; Kaastra, J.S.

Citation

Ebrero, J., Domček, V., Kriss, G. A., & Kaastra, J. S. (2021). Multi-epoch properties of the warm absorber in the Seyfert 1 galaxy NGC 985. *Astronomy And Astrophysics*, 653.
doi:10.1051/0004-6361/202040045

Version: Accepted Manuscript

License: [Leiden University Non-exclusive license](#)

Downloaded from: <https://hdl.handle.net/1887/3250967>

Note: To cite this publication please use the final published version (if applicable).

Multi-epoch properties of the warm absorber in the Seyfert 1 galaxy NGC 985

J. Ebrero¹, V. Domček^{2,3,4}, G. A. Kriss⁵, and J. S. Kaastra^{6,7}

¹ Telespazio UK for the European Space Agency (ESA), European Space Astronomy Centre (ESAC), Camino Bajo del Castillo, s/n, E-28692 Villanueva de la Cañada, Madrid, Spain
e-mail: jebroero@sciops.esa.int

² Anton Pannekoek Institute for Astronomy, University of Amsterdam, Science Park 904, 1098 XH Amsterdam, The Netherlands

³ GRAPPA, University of Amsterdam, Science Park 904, 1098 XH Amsterdam, The Netherlands

⁴ Department of Theoretical Physics and Astrophysics, Masaryk University, Kotlářská 2, 61137, Czech Republic

⁵ Space Telescope Science Institute, 3700 San Martin Drive, Baltimore, MD 21218, USA

⁶ SRON Netherlands Institute for Space Research, Sorbonnelaan 2, 3584 CA Utrecht, The Netherlands

⁷ Leiden Observatory, Leiden University, P. O. Box 9513, 2300 RA Leiden, The Netherlands

Received <date>; accepted <date>

ABSTRACT

Context. NGC 985 was observed by *XMM-Newton* twice in 2015, revealing that the source was coming out from a soft X-ray obscuration event that took place in 2013. These kinds of events are possibly recurrent since a previous *XMM-Newton* archival observation in 2003 also showed signatures of partial obscuration.

Aims. We have analyzed the high-resolution X-ray spectra of NGC 985 obtained by the Reflection Grating Spectrometer (RGS) onboard *XMM-Newton* in 2003, 2013, and 2015 in order to characterize the ionized absorbers superimposed to the continuum and to study their response as the ionizing flux varies.

Methods. The spectra were analyzed with the SPEX fitting package and the photoionization code CLOUDY.

Results. We found that up to four warm absorber (WA) components were present in the grating spectra of NGC 985, plus a mildly ionized ($\log \xi \sim 0.2 - 0.5$) obscuring ($N_{\text{H}} \sim 2 \times 10^{22} \text{ cm}^{-2}$) wind outflowing at $\sim -6000 \text{ km s}^{-1}$. The absorbers have a column density that ranges from $\sim 10^{21}$ to a few times 10^{22} cm^{-2} , and ionization parameters ranging from $\log \xi \sim 1.6$ to ~ 2.9 . The most ionized component is also the fastest, moving away at $\sim -5100 \text{ km s}^{-1}$, while the others outflow in two kinematic regimes, ~ -600 and $\sim -350 \text{ km s}^{-1}$. These components showed variability at different time scales in response to changes in the ionizing continuum. Assuming that these changes are due to photoionization and recombination mechanisms, we have obtained upper and lower limits on the density of the gas. We used these limits to pinpoint the location of the warm absorbers, finding that the closest two components are at parsec-scale distances, while the rest may extend up to tens of parsecs from the central source. With these constraints on the density and location, we found that the fastest, most ionized WA component accounts for the bulk of the kinetic luminosity injected back into the interstellar medium (ISM) of the host galaxy, which is on the order of 0.8% of the bolometric luminosity of NGC 985. According to the models, this amount of kinetic energy per unit time would be sufficient to account for cosmic feedback.

Conclusions. Observations of the onset and conclusion of transient obscuring events in active galactic nuclei (AGN) are a key tool to understand both the dynamics and physics of the gas in their innermost regions, and also to study the response of the surrounding gas as the ionizing continuum varies.

Key words. X-rays: galaxies – galaxies: active – galaxies: Seyfert – galaxies: individual: NGC 985 – techniques: spectroscopic

1. Introduction

Gravitational accretion of matter onto the supermassive black hole (SMBH) that resides in the center of most, if not all, galaxies is what powers active galactic nuclei (AGN, Rees 1984). This very efficient process produces large amounts of energy across the entire spectrum that can be detected at cosmological distances. Not only is radiation emitted, but also large amounts of matter are injected back into the interstellar medium (ISM) of the host galaxy. This process is known as feedback, and it is believed to play a major role in the coevolution of the SMBH and the galaxy (Di Matteo et al. 2005; Hopkins & Elvis 2010).

More than half of the observed type-1 AGN present signatures of photoionized gas in their soft X-ray spectrum, the so-called warm absorbers (WA), that are seen as absorption features superimposed to the continuum (e.g., Reynolds 1997;

George et al. 1998; Crenshaw et al. 2003). With the advent of high-resolution X-ray spectroscopy after the launch of *XMM-Newton* and *Chandra*, it was observed that these absorbers were blueshifted with respect to the rest frame of their host galaxy, typically by hundreds to thousands of km s^{-1} (Kaastra et al. 2000; Kaspi et al. 2001). Since they were outflowing, they were injecting kinetic energy and mass back into the ISM and therefore they were potential candidates to be a source of cosmic feedback. It is now considered that the regular WAs have, in general, little impact on their surroundings, with the exception of their most extreme version: outflows with very high velocity, ionization state, and column density, known as ultra-fast outflows (UFOs), which can have a significant impact on their host galaxy (Tombesi et al. 2012, 2013; Laha et al. 2016).

The dominant launching mechanism of these outflows is still a matter of debate as they present a wide range of velocities,

degrees of ionization, and column densities. They range from thermal winds arising from the inner edge of the torus, which is eroded by the intense radiation field (Krolik & Kriss 2001), and winds launched from the accretion disk by radiative means (Proga & Kallman 2004) or magnetohydrodynamical mechanisms (Königl & Kartje 1994; Fukumura et al. 2010a,b). In addition to this, after many years of observations and monitoring of AGN, another type of transient wind has been identified and studied: high-column density, fast, obscuring winds that eclipse the inner X-ray source of AGN on relatively short time scales. A number of objects have now shown this kind of transient phenomenon, for instance NGC 1365 (Risaliti et al. 2007), Mrk 766 (Risaliti et al. 2011), Mrk 335 (Longinotti et al. 2013, 2019), NGC 5548 (Kaastra et al. 2014), NGC 3783 (Mehdipour et al. 2017), and now also NGC 985 (Ebrero et al. 2016a).

NGC 985, also known as Mrk 1048, is a nearby ($z = 0.043$, Fisher et al. 1995), bright ($F_{0.3-10 \text{ keV}} = 2.2 \times 10^{-11} \text{ erg cm}^{-2} \text{ s}^{-1}$, Ebrero et al. 2016a) Seyfert 1 galaxy with a distinctive ring shape, produced by a recent galactic merger. This source is known to host a WA in X-rays (Krongold et al. 2005, 2009) as well as an UV absorber (Arav 2002). During a *Swift* monitoring program in 2013, the source was found to be in a very low soft X-ray flux state. A triggered joint *XMM-Newton* and HST observation found that some intervening very dense gas was occulting the central X-ray source (Parker et al. 2014). In the most recent observations in 2015, taken 12 days apart also with *XMM-Newton* and HST, we found that the source was emerging from this obscured state. The first analysis of the X-ray broad band and UV spectra were presented in Ebrero et al. (2016a). In this work we focus on the analysis of the high-resolution X-ray spectra taken by the RGS onboard *XMM-Newton* in 2015 and in the previous archival observations of this source.

This paper is organized as follows. In Sect. 2 we described the observations used in this work and the data reduction. In Sect. 3 we construct and absorbed and unabsorbed spectral energy distributions (SED) that will be used in the data analysis in Sect. 4. Our results are described and discussed in Sect. 5 and 6, respectively. Finally, we summarize our findings in Sect. 7. We adopt a cosmological framework with $H_0 = 70 \text{ km s}^{-1} \text{ Mpc}^{-1}$, $\Omega_M = 0.3$, and $\Omega_\Lambda = 0.7$. The quoted errors refer to 68.3% confidence level unless otherwise stated.

2. Observations and data reduction

In this paper we focus on the analysis of the high-resolution grating spectra of NGC 985 obtained by the *XMM-Newton* Reflection Grating spectrometer (RGS; den Herder et al. 2001). We use the same observations as in Ebrero et al. (2016a), where the EPIC-pn data were analyzed: one observation in 2003 (ObsID 0150470601), one in 2013 (ObsID 0690870501), and two in 2015 (ObsIDs 0743830501 and 0743830601, respectively). Another observation in 2013 (ObsID 0690870101) was too short (~ 20 ks of exposure time) to provide an RGS spectrum with enough signal-to-noise, and therefore it was discarded from the present analysis. The observations were retrieved from the *XMM-Newton* Science Archive (XSA¹) and re-processed using SAS v16.0 (Gabriel et al. 2004).

The RGS data were taken in the normal spectroscopy mode, and they were processed using *rgsproc* with cross-dispersion and CCD pulse-height selections of 95 per cent, and background exclusion of 98 per cent (the SAS default settings). The spectra were binned in beta space and the response matrix used 9 000

Table 1. *XMM-Newton* observations log of NGC 985.

ObsID	Obs. Date (yyyy-mm-dd)	Start Time (hh:mm:ss)	Exp. Time (ks)
0150470601	2003-07-15	15:28:36	57.9
0690870501	2013-08-10	21:17:52	103.7
0743830501	2015-01-13	09:52:59	138.9
0743830601	2015-01-25	08:48:22	122.0

bins. The observations and their exposure times are summarized in Table 1.

3. Obscured and unobscured spectral energy distributions

The spectral energy distributions (SED) of the observations were constructed using the contemporaneous measurements of *XMM-Newton* EPIC-pn in the X-rays, HST in the UV (except for the 2003 observation in which no contemporaneous HST data were available), and the *XMM-Newton* optical monitor (OM) in the UV and optical band. Following the results of Ebrero et al. (2016a), where it is shown that the central ionizing source is partially blocked by obscuring material, we constructed two SED sets. One is the unobscured SED (e.g., the spectrum emitted by the AGN in NGC 985) and the other one is the obscured SED, filtered by the obscuring intervening material. The latter will be used in the analysis of the WA components in NGC 985, which are assumed to be located farther than the obscurer (see Sect. 4). This approach was also followed in Mehdipour et al. (2015) and Di Gesu et al. (2015) in order to analyze the outflows in NGC 5548, which was also found to be in a persistent obscured state (Kaastra et al. 2014).

In both cases the X-ray SED was obtained from the best-fit EPIC-pn model (Ebrero et al. 2016a) corrected from intrinsic and Galactic absorption. For the obscured SED we kept the obscuring component as measured in Ebrero et al. (2016a). In the UV we used the HST-COS continuum fluxes at 1175, 1339, 1510, and 1765 Å corrected for Galactic extinction using the reddening curve prescription of Cardelli et al. (1989), assuming a color excess $E(B - V) = 0.03$ mag based on calculations of Schlegel et al. (1998) as updated by Schlafly & Finkbeiner (2011), as given in the NASA/IPAC Extragalactic Database (NED²), and a ratio of total to selective extinction $R_V \equiv A_V/E(B - V)$ fixed to 3.1.

The OM observations were taken with the *V*, *B*, *U*, *UVW1*, *UVM2*, and *UVW2* filters in the 2013 and both 2015 observations, and with the *U*, *UVW1*, *UVM2*, and *UVW2* filters in the 2003 observation. The OM fluxes were also corrected for Galactic extinction using the reddening curve of Cardelli et al. (1989), including the update in the optical and near-IR of O'Donnell (1994). To correct for the host galaxy starlight contribution in the OM bandpasses we used the bulge galaxy template of Kinney et al. (1996), scaled to the host galaxy flux at the rest-frame wavelength $F_{\text{gal}, 5100 \text{ Å}} = 2.48 \times 10^{-15} \text{ erg cm}^{-2} \text{ s}^{-1} \text{ Å}^{-1}$ (Kim et al. 2008). The adopted SEDs are shown in Fig. 1.

¹ <http://nxsa.esac.esa.int/nxsa-web/>

² <http://ned.ipac.caltech.edu/>

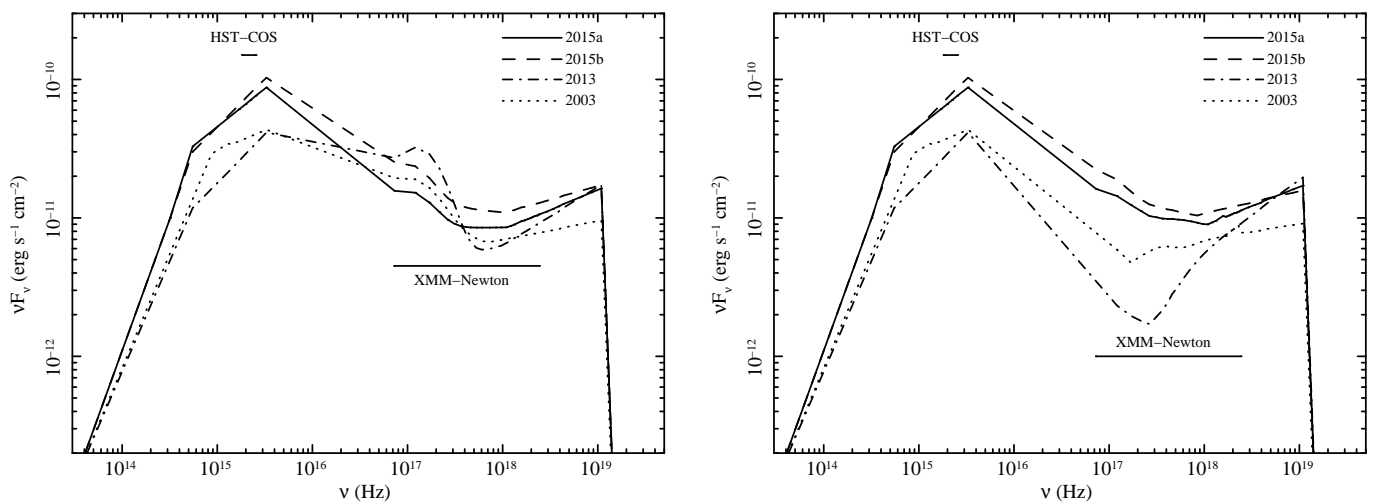


Fig. 1. Unobscured (*left panel*) and obscured (*right panel*) spectral energy distributions of the 2015a (solid line), 2015b (dashed line), 2013 (dot-dashed line), and 2003 (dotted line) observations. The bands covered by HST-COS and XMM-Newton are also indicated.

4. Data analysis

The RGS spectra of NGC 985 were analyzed using the SPEX fitting package³ version 3.05.01 (Kaastra et al. 1996). The adopted fitting method was C-statistics (Cash 1979) so that binning of the data is in principle no longer needed. However, to avoid oversampling, we rebinned by a factor of 5 in the 7 – 24 Å range, and by a factor of 7 in the 24 – 38 Å range, in order to compensate for lower effective area and therefore higher noise toward lower energies in the individual 2015 observations. The 2003 and 2013 observations, affected by a lower signal-to-noise due to the presence of the obscurer and shorter exposure time (in 2003), were analyzed only in the region 7 – 26 Å, rebinned by a factor of 7. The foreground Galactic column density was set to $N_{\text{H}} = 3.17 \times 10^{20} \text{ cm}^{-2}$ (Kalberla et al. 2005) using the *hot* model in SPEX, with the temperature fixed to 0.5 eV to mimic a neutral gas. Throughout the analysis we adopted a cosmological redshift of $z = 0.043$ (Fisher et al. 1995), and we assumed the proto-Solar abundances of Lodders & Palme (2009).

4.1. Continuum and emission lines

The continuum was modeled locally in the RGS waveband with a single powerlaw with the photon index Γ fixed to the values obtained in the analysis of the EPIC-pn spectra of Ebrero et al. (2016a). The soft excess was modeled using a modified black body (*mbb* model in SPEX), which takes into account modifications of a simple black body model by coherent Compton scattering based on the calculations of Kaastra & Barr (1989). The best-fit values of the continuum parameters for the different observations are reported in Table 2.

In addition, the RGS spectra showed the presence of some narrow emission lines sticking out of the continuum. These emission features were modeled with Gaussian line models with centroid wavelengths fixed to the laboratory wavelength at the rest-frame of the source. The most prominent line seen in all of the observations was the He-like forbidden O VII line. In the 2013 observation, the depressed continuum due to the ongoing obscuration allowed to significantly detect emission features from other species and transitions. H-like Ly α transitions of O VIII and Mg XII were significantly detected in this observation, whereas

that of N VII was below the 2σ level. The He-like forbidden line of Ne IX was detected above the 4σ level, whereas the He-like forbidden line of Mg XI was less significant but still detected at the 3σ . The O VII intercombination line was detected at the 2σ level or higher in the 2003, 2013, and in the 2015a observation, while in the 2015b observation it was not significantly detected, owing to the higher continuum. We also detected the resonance line of He-like O VII, above the 6σ level, which was also found with less significance in the 2015b observation. Overall, the detection prominent forbidden lines together with slightly weaker resonance lines suggests that these lines originate in a photoionized plasma (Porquet & Dubau 2000). The list of emission lines detected in the RGS spectra of NGC 985 together with their line fluxes and detection significance are reported in Table 3.

In this Table we also show the laboratory wavelength and the measured best-fit, rest-frame centroid wavelengths for each transition. There is no evident connection between the emitting medium and the absorbers described in Sect. 4.2. The vast majority of the best-fit values are consistent with the laboratory ones, or slightly blueshifted with negligible significance (typically less than 1σ). The gas responsible for the emission lines is therefore not outflowing. Furthermore, the majority of the detected emission lines are narrow, unresolved lines. The most prominent of these lines, detected in all four observations, do not show changes in their widths. All of this implies that the emitting material is likely located much further away than the absorbers.

4.2. Absorption features

NGC 985 is known to host an intrinsic WA in the form of ionized winds with multiple ionization phases (Krongold et al. 2005; Krongold et al. 2009). Indeed, the RGS spectra show a plethora of absorption troughs that can be attributed to intervening ionized gas at the redshift of the source. We modeled the absorption features in our spectra using the model *xabs* in SPEX, which calculates the transmission through a slab of material where all the ionic column densities are linked through a photoionization balance model. The latter was provided to *xabs* as an input, and it was calculated with CLOUDY⁴ v13.01 (Ferland et al. 2013) using as inputs the SEDs shown in Sect 3. For the fits we left as free parameters in *xabs* the ionization parameter ξ , the hydrogen

³ <http://www.sron.nl/astrophysics-spx>

⁴ <http://www.nublado.org>

Table 2. Best-fit continuum parameters.

Model	Parameter	Obs. 2003	Obs. 2013	Obs. 2015a	Obs. 2015b
Power-law	$F_{0.2-2 \text{ keV}}^a$	$5.1^{+1.4}_{-0.8} \times 10^{-12}$	$7.3^{+3.0}_{-2.1} \times 10^{-13}$	$9.2 \pm 1.7 \times 10^{-12}$	$1.4 \pm 0.2 \times 10^{-11}$
	Γ^b	2.21	1.71	2.14	2.22
Mod. BB	$F_{0.2-2 \text{ keV}}^a$	$1.4^{+3.1}_{-1.1} \times 10^{-13}$	$7.5 \pm 0.4 \times 10^{-13}$	$1.4 \pm 0.5 \times 10^{-12}$	$2.3 \pm 0.5 \times 10^{-12}$
	T^c	0.10 ± 0.05	0.27 ± 0.04	0.12 ± 0.01	0.12 ± 0.01

Notes. ^(a) Observed flux in the 0.2 – 2 keV range, in units of $\text{erg cm}^{-2} \text{ s}^{-1}$; ^(b) power-law photon index, frozen to the EPIC-pn best-fit values of Ebrero et al. (2016a); ^(c) temperature, in units of eV.

Table 3. Emission lines in the RGS spectra of NGC 985.

Line ^a	λ_0^b	λ^c	$\Delta\lambda^d$	Flux ^e	σ^f
Obs. 2003					
O VII, aw	21.6015	21.3 ± 0.1	0.2 ± 0.1	28.0 ± 9.0	3.1
O VII, af	22.0974	22.0 ± 0.1	0.4 ± 0.2	41.0 ± 10.0	4.1
Obs. 2013					
Mg XII, L α	8.421	8.41 ± 0.04	<0.2	15.0 ± 5.0	3.0
Mg XI, af	9.3136	9.25 ± 0.04	0.2 ± 0.1	15.0 ± 5.0	3.0
Ne IX, af	13.6984	13.69 ± 0.02	<0.1	6.4 ± 1.5	4.3
O VIII, L β	16.0059	16.1 ± 0.1	0.3 ± 0.1	8.4 ± 1.7	4.9
O VII, bf	18.7307	18.08 ± 0.02	<0.2	6.2 ± 1.9	3.3
O VIII, L α	18.9689	18.96 ± 0.02	<0.2	12.0 ± 3.0	4.0
O VII, aw	21.6015	21.60 ± 0.04	0.3 ± 0.1	19.0 ± 3.0	6.3
O VII, ai	21.802	21.87 ± 0.03	<0.1	6.2 ± 3.5	1.8
O VII, af	22.0974	22.09 ± 0.01	<0.1	21.0 ± 4.0	5.3
N VII, L α	24.781	24.7 ± 0.1	0.2 ± 0.1	4.1 ± 2.6	1.6
Obs. 2015a					
O VII, ai	21.802	21.83 ± 0.03	<0.1	11.0 ± 5.0	2.2
O VII, af	22.0974	22.12 ± 0.02	<0.1	21.0 ± 5.0	4.2
C VI, L α	33.735	33.6 ± 0.1	<0.4	4.7 ± 2.9	1.6
Obs. 2015b					
O VII, aw	21.6015	21.57 ± 0.05	<0.4	23.0 ± 12.0	1.9
O VII, af	22.0974	22.10 ± 0.02	<0.2	30.0 ± 11.0	2.7
C VI, L α	33.735	33.4 ± 0.1	0.3 ± 0.1	35 ± 8.0	4.4

Notes. ^(a) Emission line transitions (L: H-like, a: He α -like, b: He β -like, w: resonance, i: intercombination, f: forbidden); ^(b) laboratory wavelength, in Å; ^(c) rest-frame wavelength, in Å; ^(d) line width, in Å; ^(e) line flux, in units of $10^{-15} \text{ erg cm}^{-2} \text{ s}^{-1}$; ^(f) significance of the detection.

column density N_{H} , the velocity width σ , and the outflow velocity v_{out} . The ionization parameter is a measure of the ionization state of the gas, and it is defined as

$$\xi = \frac{L_{\text{ion}}}{nR^2}, \quad (1)$$

where L_{ion} is the ionizing luminosity in the 1 – 1000 Ryd range, n is the hydrogen density of the gas, and R is the distance of the gas to the ionizing source.

As shown in Ebrero et al. (2016a), the obscuring material that caused the low soft X-ray flux state of the source in 2013 (Parker et al. 2014) was still present in the 2003 observation and, to a lower extent, in the 2015 observations. The obscurer is mildly ionized and its observed variability can be described solely by changes in its covering fraction (Ebrero et al. 2016a). We therefore modeled the obscurer with a *xabs* component

where, in addition to the free parameters mentioned above, we also let the covering fraction f_c free.

The fits were carried out with the following approach. We started by adding a *xabs* component for the obscurer using the ionization balance generated with the unobscured SED. Since the obscurer is likely located closer to the central engine than the regular WA, possibly close to the BLR (Ebrero et al. 2016a), it is reasonable to assume that it will be irradiated by the unobscured, intrinsic spectrum of the AGN. After this, we added additional *xabs* components to model the multi-phase WA on a one-by-one basis until the fit no longer improved. The WA *xabs* components were fed with the ionization balance generated with the obscured SED (the SED filtered by the obscurer). The progress of the fit in terms of C-stat and intermediate $\log \xi$ values is shown in Table 4. It can be seen that for the 2015 observations a total of five *xabs* components were required, one to account for the obscurer and a WA with four distinct ionization phases. The 2003 and 2013

observations, on the other hand, analyzed in the 7 – 26 Å band due to the obscured continuum at longer wavelengths, only required three and four *xabs* components, respectively: one for the obscurer and two or three WA phases. In these two observations the addition of an additional *xabs* component only produced a marginal improvement in the fit, $\Delta(C - \text{stat})/\Delta(\text{d.o.f.}) = 7/4$ in 2003 and $\Delta(C - \text{stat})/\Delta(\text{d.o.f.}) = 5/4$ in 2013, respectively. The resulting best-fit parameters are reported in Table 5. The RGS spectrum of the second observation in 2015 is shown in Fig. 2. The remaining spectra used in this work are shown in Appendix A.

5. Results

5.1. The obscurer

NGC 985 experienced a low soft X-ray flux state in 2013 which was attributed to the passing by of an obscuring cloud of material across our line of sight (Parker et al. 2014). The analysis of the *XMM-Newton* EPIC-pn spectra of NGC 985 revealed that this obscuration event was possibly recurrent since there were signatures of obscuration in 2003, followed by an unobscured period in 2007–2008 (according to *Swift* monitoring), before entering in the obscuration event of 2013. Interestingly, the analysis of the 2015 *XMM-Newton* observations showed that some hints of obscuration were still present in the X-ray and UV spectra of NGC 985 (Ebrero et al. 2016a).

The results of the fits to the RGS spectra shown in Table 5 reveal that the Hydrogen column density of the obscurer remained constant throughout the observations, with $N_{\text{H}} \sim 2 \times 10^{22} \text{ cm}^{-2}$, with the exception of the 2013 observation, in which the best-fit value is ~ 3 times larger. The main consequence is that all the observed changes due to the presence of the obscurer can solely be attributed to variations in the covering fraction of this material. During the monitoring campaign of 2013 the obscurer was almost fully blocking our line of sight ($f_{\text{c}} = 0.94$), whereas in 2003 the covering fraction was almost two thirds. The inclusion of this obscurer component in the fits of the 2015 observations, when the source had a soft X-ray flux ~ 10 times higher than in 2013 and almost twice as bright as in 2003, resulted in a lower covering fraction in the first of the 2015 observations ($f_{\text{c}} = 0.49$) and a much smaller, but not negligible value in the second observation in 2015 ($f_{\text{c}} = 0.18$), as shown in Fig. 3.

These covering fraction variations can be interpreted in the context of various possible scenarios. In one of them the obscurer is most likely clumpy so that a fraction of the continuum emission is leaking through it. The different covering fractions observed could indicate that our line of sight is pointing toward the edge of the outflow in the 2003 and 2015 observations, while in 2013 it is intercepting the bulk of the obscuring wind. Another point is related to the duration of the obscuring events. The recurrent appearance and disappearance of the obscurer may indicate that it is transient, although the possibility that it is launched in the form of a continuous stream of gas cannot be ruled out. In the latter case, the intrinsic motion of the wind in the proximity of the central engine would make the outflow intersect our line of sight and drift away from it at the different epochs. An extreme case of this situation would be the long-lasting obscuration event in NGC 5548, which has persistently been in this state for the last several years (Mehdipour et al. 2016).

5.2. The warm absorber

The soft X-ray spectra of NGC 985 show several absorption troughs associated with intervening ionized winds outflowing at different kinematic regimes. The best-fit results of the higher signal-to-noise *XMM-Newton* RGS spectra in 2015 revealed that these outflows are composed of four components with distinct ionization states, although the actual values of $\log \xi$ seem to fluctuate between the different observations. This will be discussed in detail in Sect. 6.2.

All of the WA components show deep Hydrogen column densities N_{H} , ranging from $\sim 10^{21}$ to a few times 10^{22} cm^{-2} . The highest ionization component *A*, with $\log \xi_{\text{A}} \sim 2.9$, is also the fastest, outflowing at $\sim -5100 \text{ km s}^{-1}$. The slowest WA component *C*, with $\log \xi_{\text{C}} \sim 2.0$, is moving at $\sim -350 \text{ km s}^{-1}$, while the remaining components *B* ($\log \xi_{\text{B}} \sim 2.6$) and *D* ($\log \xi_{\text{D}} \sim 1.6$) are kinematically more difficult to disentangle, both traveling at around -650 km s^{-1} and -560 km s^{-1} , respectively, with overlapping error bars. The measured turbulent velocity σ is also mostly consistent across observations. In some cases, such as components *A* and *C* in 2013, σ appears to adopt higher values but with very large associated uncertainties.

The observations of 2003 and 2013, affected by the shorter exposure times and the flux suppression due to the presence of the obscurer, had a worse signal-to-noise ratio and could only be analyzed in the 7 – 26 Å band. Only two WA components could be significantly detected in 2003, and three in 2013. Their cross-identification with the WA phases in the 2015 observations was not straightforward in some cases. For instance, for the two WA components detected in the 2003 observation, the one with $\log \xi = 1.82$ outflowing at -385 km s^{-1} was immediately cross-identified with component *C* in the 2015 observations since its kinematic properties and column density matched well those of 2015, albeit with a somewhat lower ionization parameter. The other WA component was identified with component *B* based on the similar column density and ionization parameter as those in 2015, although their kinematics were difficult to reconcile with those of that component in 2015. The measured outflow velocity of -210 km s^{-1} was smaller than the outflow velocity measured in 2015 for this component, $\sim -650 \text{ km s}^{-1}$, but the large error bars in the former make these values consistent within less than 2σ .

The three components detected in the 2013 observation, the most affected by the obscuration, were also difficult to cross-identify with their counterparts in 2015 in some cases. Two of them were identified with component *A* and *B*, based on their similarities in kinematics and column densities. The third component was identified as component *D*, based on the measured column density. It is worth noting that all the detected components in the 2013 observations seem to be kinematically faster with respect to their counterparts in 2015. The measured outflow velocity in components *B*, *D*, and in the obscurer itself have such large uncertainties that are consistent within 1σ with the velocities seen in 2015. The only exception is component *A*, which seems to be significantly faster in 2013. Typical accelerations (or decelerations) due to radiation pressure at those distances make it difficult to reconcile such values. While the possibility that we are detecting another, different kinematic component is also a reasonable explanation for this disparity, the fact that all components seem to be faster (albeit the large uncertainties in most of the cases) may indicate that some other systematic process is in action. A change in the projected outflow velocity may also indicate a change in the angle subtended between the outflow and our line of sight. However, for a change of about 30% in ve-

Table 4. Progress of the fit after including an additional warm absorber component in each iteration. The values refer to the ionization parameter $\log \xi$ in each *xabs* component. The values in bold are those of the obscurer. The underlined values are the adopted best-fit values.

Obs. 2003 (d.o.f. = 394)			Obs. 2013 (d.o.f. = 359)		
Model	C-stat	$\log \xi$	C-stat	$\log \xi$	
0xabs	840	-	645	-	
1xabs	524	1.15	525	0.78	
2xabs	468	2.39, 1.04	474	1.96, 1.61	
3xabs	<u>448</u>	2.44, 1.82, 1.07	462	1.95, 1.05, 1.67	
4xabs	<u>452</u>	2.01, 2.51, 1.01, 1.68	
Obs. 2015a (d.o.f. = 854)			Obs. 2015b (d.o.f. = 853)		
Model	C-stat	$\log \xi$	C-stat	$\log \xi$	
0xabs	2939	-	3147	-	
1xabs	1844	1.17	1843	1.43	
2xabs	1610	2.63, 1.18	1620	2.80, 1.44	
3xabs	1135	2.82, 2.13, 0.98	1281	2.94, 2.13, 1.34	
4xabs	1038	2.82, 2.56, 1.95, 0.79	1127	2.91, 2.93, 2.00, 0.72	
5xabs	<u>1028</u>	2.84, 2.58, 2.01, 1.64, 0.90	<u>1056</u>	2.93, 2.93, 2.04, 1.49, 0.92	

Table 5. Best-fit values for the obscurer (Component *O*) and WA (Components *A* to *D*) in NGC 985.

Component	Parameter	Obs. 2003	Obs. 2013	Obs. 2015a	Obs. 2015b
<i>O</i>	N_{H}^a	$2.6 \pm 0.8 \times 10^{22}$	$7.8 \pm 1.8 \times 10^{22}$	$2.8 \pm 0.6 \times 10^{22}$	$1.3 \pm 0.8 \times 10^{22}$
	f_c^b	0.62 ± 0.06	0.94 ± 0.01	0.49 ± 0.09	0.18 ± 0.07
	$\log \xi^c$	$1.07^{+0.04}_{-0.11}$	1.68 ± 0.05	0.90 ± 0.17	$0.92^{+0.42}_{-0.59}$
	σ^d	590 ± 140	1800 ± 1500	100^{+160}_{-60}	110^{+150}_{-70}
	v_{out}^e	-6820 ± 340	-11400 ± 3200	-6450 ± 280	-5200^{+600}_{-370}
<i>A</i>	N_{H}^a	...	$1.3 \pm 0.2 \times 10^{22}$	$1.6^{+3.1}_{-0.8} \times 10^{22}$	$2.3^{+2.4}_{-1.1} \times 10^{22}$
	$\log \xi^c$...	2.01 ± 0.05	2.84 ± 0.03	2.93 ± 0.03
	σ^d	...	35^{+30}_{-10}	60^{+55}_{-40}	< 20
	v_{out}^e	...	-7200^{+300}_{-60}	-5100 ± 100	-5100^{+150}_{-50}
<i>B</i>	N_{H}^a	$2.0^{+1.7}_{-0.7} \times 10^{22}$	$2.3^{+2.9}_{-1.0} \times 10^{22}$	$3.6 \pm 1.2 \times 10^{22}$	$1.0 \pm 0.6 \times 10^{23}$
	$\log \xi^c$	2.44 ± 0.08	2.51 ± 0.06	2.58 ± 0.06	2.93 ± 0.02
	σ^d	80^{+60}_{-30}	400 ± 250	< 20	30 ± 10
	v_{out}^e	-210^{+230}_{-170}	-600^{+500}_{-350}	-700 ± 60	-640^{+100}_{-30}
<i>C</i>	N_{H}^a	$5.7 \pm 1.5 \times 10^{21}$...	$4.9 \pm 0.7 \times 10^{21}$	$5.7 \pm 0.4 \times 10^{21}$
	$\log \xi^c$	1.82 ± 0.05	...	2.01 ± 0.04	2.04 ± 0.02
	σ^d	60^{+50}_{-30}	...	95 ± 25	125 ± 15
	v_{out}^e	-385^{+240}_{-115}	...	-365 ± 45	-350 ± 30
<i>D</i>	N_{H}^a	...	$1.5 \pm 0.5 \times 10^{21}$	$1.0 \pm 0.6 \times 10^{21}$	$1.0 \pm 0.3 \times 10^{21}$
	$\log \xi^c$...	1.01 ± 0.17	1.64 ± 0.14	1.49 ± 0.09
	σ^d	...	60 ± 40	65^{+80}_{-30}	85^{+45}_{-30}
	v_{out}^e	...	-920^{+420}_{-150}	-560 ± 75	-580 ± 75
C-stat/d.o.f.		440/394	452/359	1028/854	1056/853

Notes. ^(a) Hydrogen column density, in units of cm^{-2} ; ^(b) covering fraction; ^(c) ionization parameter, in units of erg cm s^{-1} ; ^(d) velocity width, in units of km s^{-1} ; ^(e) outflow velocity, in units of km s^{-1} .

locity, if solely explained by this, the angle of the outflow may have changed by almost 45 degrees with respect to the line of sight. Such a bent is somewhat extreme, and it seems difficult to explain how can it happen in timescales of tens of months. The poor statistics, however, do not allow us to explore any of these scenarios in further detail. Furthermore, in all cases, the measured ionization parameter in 2013 is significantly lower than

those of their 2015 counterparts, possibly indicating a change in the ionization properties of the WA in response to the dramatic suppression of the ionizing flux (see Sect. 6.2).

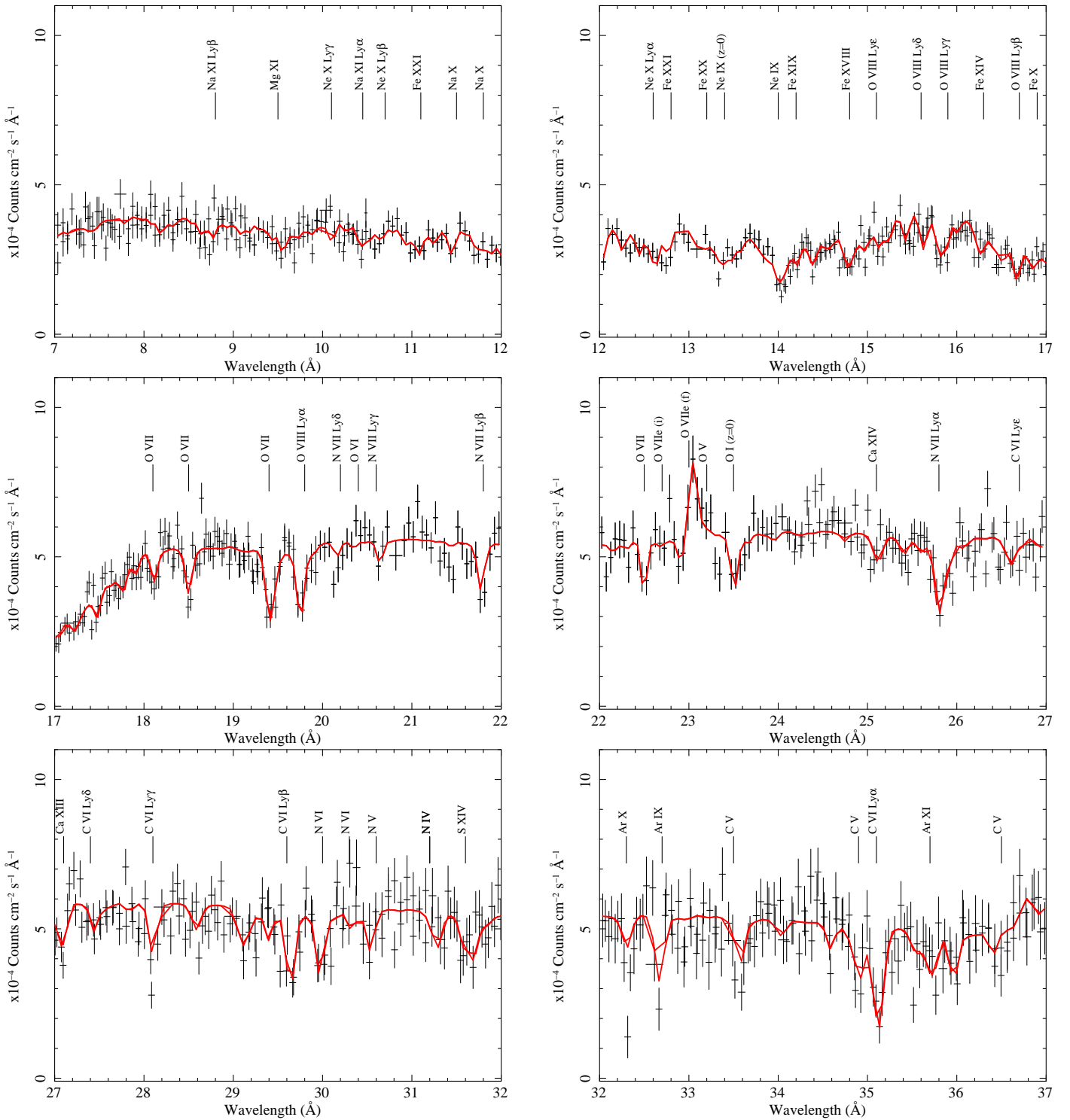


Fig. 2. *XMM-Newton* RGS spectrum of NGC 985 in 2015 (second observation). The solid red line represents the best fit model. The most relevant features have been labeled.

6. Discussion

6.1. Thermal stability

The thermal stability curves of a photoionized gas, also known as cooling curves or S-curves, provide some insight into the structure of the absorbers. The shape of these curves is determined by the SED that illuminates the gas, and they usually represent the pressure ionization parameter Ξ as a function of the electron

temperature T (Krolik et al. 1981). The pressure ionization parameter is defined as:

$$\Xi = L/4\pi r^2 c p = \xi/4\pi c k T, \quad (2)$$

where ξ is the ionization parameter as defined in Eq. 1, c is the speed of light, k is the constant of Boltzmann, and T is the electron temperature. We computed the different values of Ξ in each of the four *XMM-Newton* observations by feeding CLOUDY

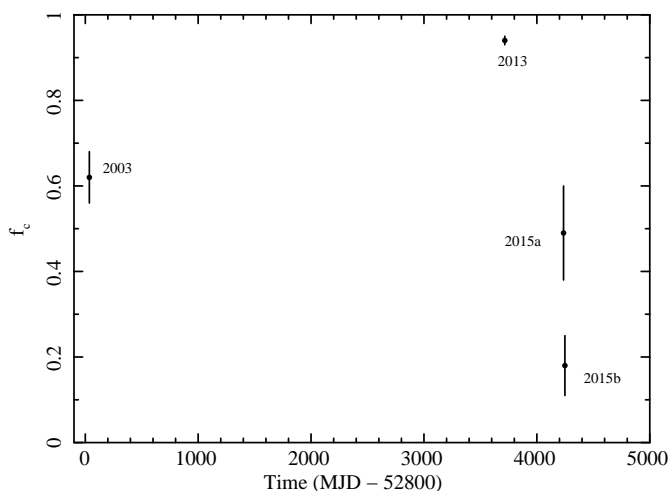


Fig. 3. Covering fraction f_c of the obscurer in the different *XMM-Newton* observations.

v13.01 with their corresponding SEDs (described in Sect. 3) and assuming the proto-Solar abundances of Lodders & Palme (2009). The output was a grid of ionization parameters ξ and their corresponding temperature T for a thin layer of gas irradiated by the ionizing continuum. These curves, shown in Fig. 4, divide the $\Xi - T$ plane in two regions: above the curve cooling dominates heating, while below the curve heating dominates cooling. Over the points on the curve the cooling rate equals the heating rate, and the gas is therefore in thermal equilibrium. The branch of the curves with negative derivative $d\Xi/dT < 0$, where the curve turns backwards, represent a region in the $\Xi - T$ space which is unstable against isobaric perturbations. As a result, a parcel of gas located in this area that is subject to a small positive temperature perturbation will see its temperature to increase until it reaches the next stable branch (those with positive derivative $d\Xi/dT > 0$). In turn, a negative temperature perturbation will lead to a temperature decrease until the parcel of gas falls to a stable branch.

We have overplotted the WA components, as well as the obscurer, detected in each of the observations over their respective stability curve. The WA components are shown in Fig. 4 as red squares, and the obscurer is represented by a blue triangle. Owing to its mild ionization level, the obscurer is located in the stable branch at the bottom of the curve in all of the observations, sharing this space with component *D* and, to a lesser extent, with Component *C*. This component *C*, when detected, is located at the edge of this branch, just before the curve turns backwards. Component *B*, on the other hand, is always located in the unstable branch of the curve, changing its position slightly as its ionization state changes in the different epochs. Component *A* is co-located with component *B* in the 2015 observations. In 2013, when the source was most obscured, its ionization parameter decreased by almost 1 dex, and thus this component slid down the curve to the stable branch. Unfortunately, this component was not detected in the 2003 observation and therefore we cannot know its behavior prior to the obscured phase.

Stability curves are also useful to probe whether the different ionized phases are in pressure equilibrium, when they share the same Ξ . For these observations, however, because of the large uncertainties in several parameters, this kind of analysis is somewhat difficult. Nevertheless, some rough conclusions might be drawn from these plots. The WA components seem to be scattered over the plots but may be divided in two blocks, one with

the highest ionization components *A* and *B*, and another one with the less ionized components *C* and *D*. Each of these blocks are in principle not in pressure equilibrium with each other, while within each block the pairs of components are within their respective errors. For example, components *A* and *B* are both quite close to each other on the unstable branch of the S-curve in the 2015 observations. The exception to this was in the 2013 observation when component *A* was significantly less ionized. On the other hand, components *C* and *D* share a similar locus in the stable branch, together with the obscurer.

This broad division is at odds with the results of Krongold et al. (2005) and Krongold et al. (2009). They found that the high- and low-ionization phases (that can be assimilated to each of the blocks described here) were in pressure equilibrium. Their main conclusion is that this components were co-located, or embedded one into another, or that they both were embedded in a third, nondetected, component. This discrepancy can be explained by the different shapes of the stability curves between those works and this one. Krongold et al. (2005) used *Beppo-SAX* and *Chandra* data from 1999 and 2002, when NGC 985 was only mildly obscured (see Fig. 6 in Ebrero et al. 2016a), and Krongold et al. (2009) used the *XMM-Newton* 2003 observation. If the obscurer is not taken into account when creating the SED, together with the different performances of photoionization codes over time (Ebrero et al. 2016b), this may lead to a different S-curve shape and a different location of the components on it which can explain the discrepancy.

Interestingly, from the results in Table 5 and the plots in Fig. 4 it is immediately noticeable the similarity in the kinematics between the obscurer and the WA component *A*, both out-flowing at comparable velocities, and in their column densities. They also share similar Ξ values, consistent within 1σ , in the S-curves which would mean they are pressure equilibrium, being almost co-located in 2013, when the source was most obscured. The question that arises is whether both absorbers are part of the same long-lived structure. If they are, a plausible scenario that can explain the changes in component *A* and in the obscurer is that the latter is confined by the former. In this case, when the flux drops component *A* becomes less ionized and the pressure dramatically decreases, as seen in the 2013 observation. Since this component is in an unstable branch of the curve a perturbation that lowers its temperature would make it travel down the curve until a stable branch is reached. To compensate for this pressure drop, the obscurer must expand, lowering its density and, in turn, increasing its ionization parameter (Krongold et al. 2005). As the flux rises back again during the 2015 observations the process reverts. While this explains the observed behavior, it requires the components to be in ionization equilibrium; otherwise the components would not even need to be located on the stability curve. Furthermore, the different velocity widths may indicate that the obscurer and component *A* are not co-located (but also see Sect. 6.3). From the UV analysis, given that only $\sim 25\%$ of the UV emitting area is obscured while the X-ray emission almost fully obscured, it is likely that the obscurer is much closer to the central source, possibly in or near the BLR (Ebrero et al. 2016a; Kriss et al., in preparation).

6.2. Variability

If the changes observed in the WA components are due to photoionization and recombination of the ionized gas in response to

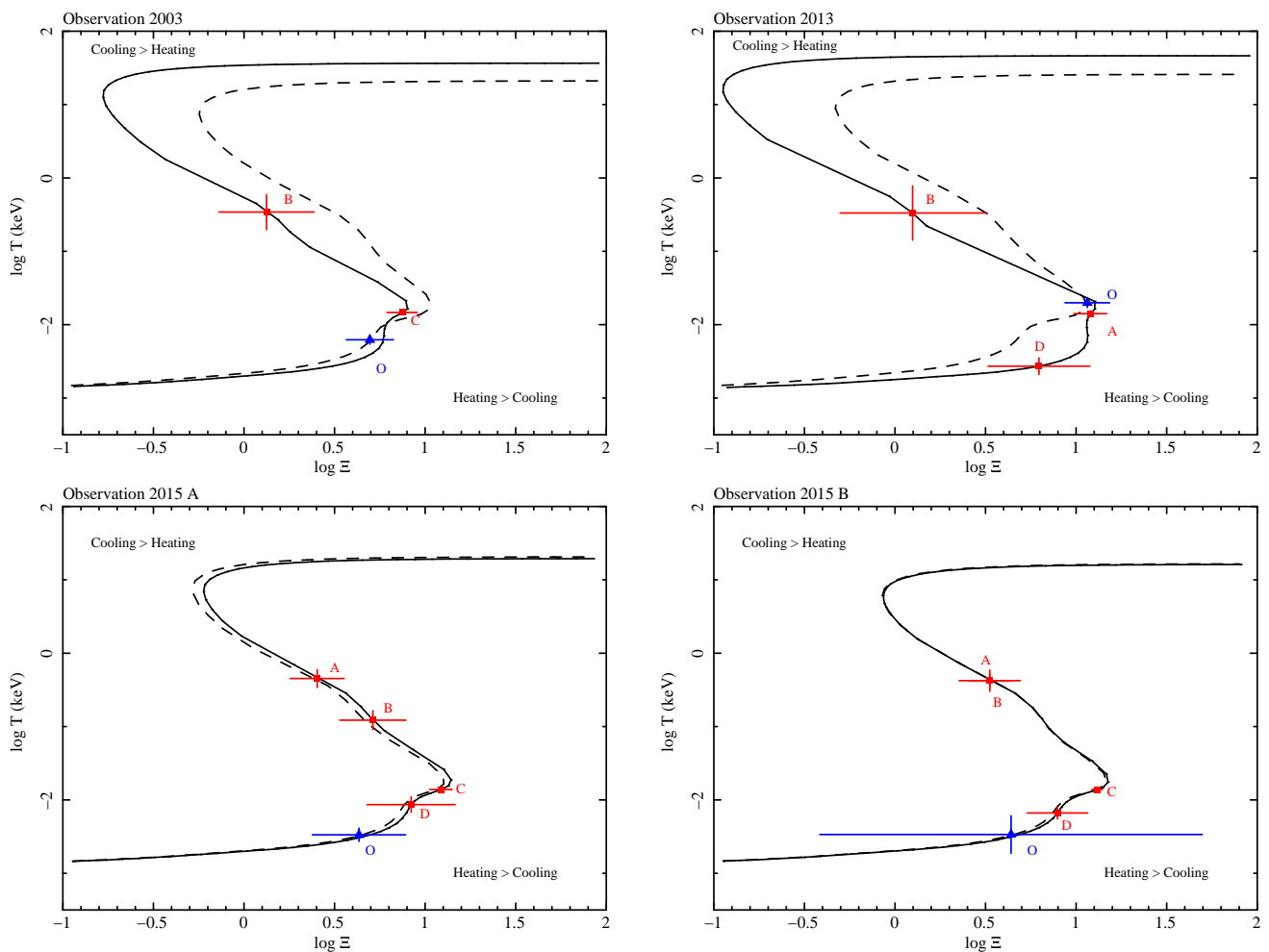


Fig. 4. Pressure ionization parameter as a function of the electron temperature for the unobscured (dashed line) and obscured (solid line) SEDs in the 2003 (*top left panel*), 2013 (*top right panel*), and the 2015 observations (*bottom panels*). The X-ray WA components are represented with filled red squares (A to D) and the obscurer (O) is represented with a filled blue triangle.

the ionizing flux variations, a lower limit on the density of the absorbing gas can be estimated using (Bottorff et al. 2000):

$$t_{\text{rec}}(X_i) = \left(\alpha_r(X_i) n \left[\frac{f(X_{i+1})}{f(X_i)} - \frac{\alpha_r(X_{i-1})}{\alpha_r(X_i)} \right] \right)^{-1}, \quad (3)$$

where $t_{\text{rec}}(X_i)$ is the recombination time scale of a given ion X_i , $\alpha_r(X_i)$ is the recombination rate from ion X_{i-1} to ion X_i , and $f(X_i)$ is the fraction of element X at the ionization level i . The recombination rates α_r of the different ions are known from the atomic physics, while the fractions f can be determined from the ionization balance of the source. Therefore, for a given ion X_i it is possible to obtain a lower limit on the density n if an upper limit on the recombination time t_{rec} is known, since $t_{\text{rec}} \propto 1/n$. One has to keep in mind, however, that the estimations obtained with the formula above will hold under the assumption that the gas has reached equilibrium again.

The observations analyzed in this paper allow us to probe time scales that range between 12 days to almost 12 years. We followed a similar approach as in Ebrero et al. (2016b), and we calculated the measured variation in the ionization parameter ξ between each individual observation. In this way we can explore the typical time scales at which the different WA components begin to vary. The sampling of the observations is, however,

sparse. We cover an ample range of time scales, but at the expense of lacking enough high-resolution spectra at intermediate epochs. This is of course unavoidable, as the investment in observing time for one AGN would be prohibitive otherwise. Each of these observations is a snapshot in the behavior of the ionized absorbers. The observed changes are then assumed to have happened some time between observations, but when exactly is uncertain. The results of this exercise are shown in Fig. 5. It can be seen that component A begin to significantly vary at time scales of ~ 520 days. Component B, on the other hand, already showed signs of variability in the ~ 12 days spanned between the 2015 observations. Components C and D show some variability, but below the 2σ level, at around 4200 and 520 days.

The fraction of a given element X in an ionization state i , $f(X_i)$ in Eq. 3, can be determined from the ionization balance of NGC 985. It provides the ionic column densities of the different elements that can be divided by the total hydrogen column density to obtain $f(X_i)$. We identified the ions that contributed most to each WA component based on their column density, oscillator strength, and significance of their spectral features, so that they are the drivers of the fit. We then passed the ionic column densities of these ions to the SPEX auxiliary program *rec_time*, that provides as output the product nt_{rec} for each of them. The tables with the ions used as a proxy for each WA component and their nt_{rec} product are listed in Appendix C.

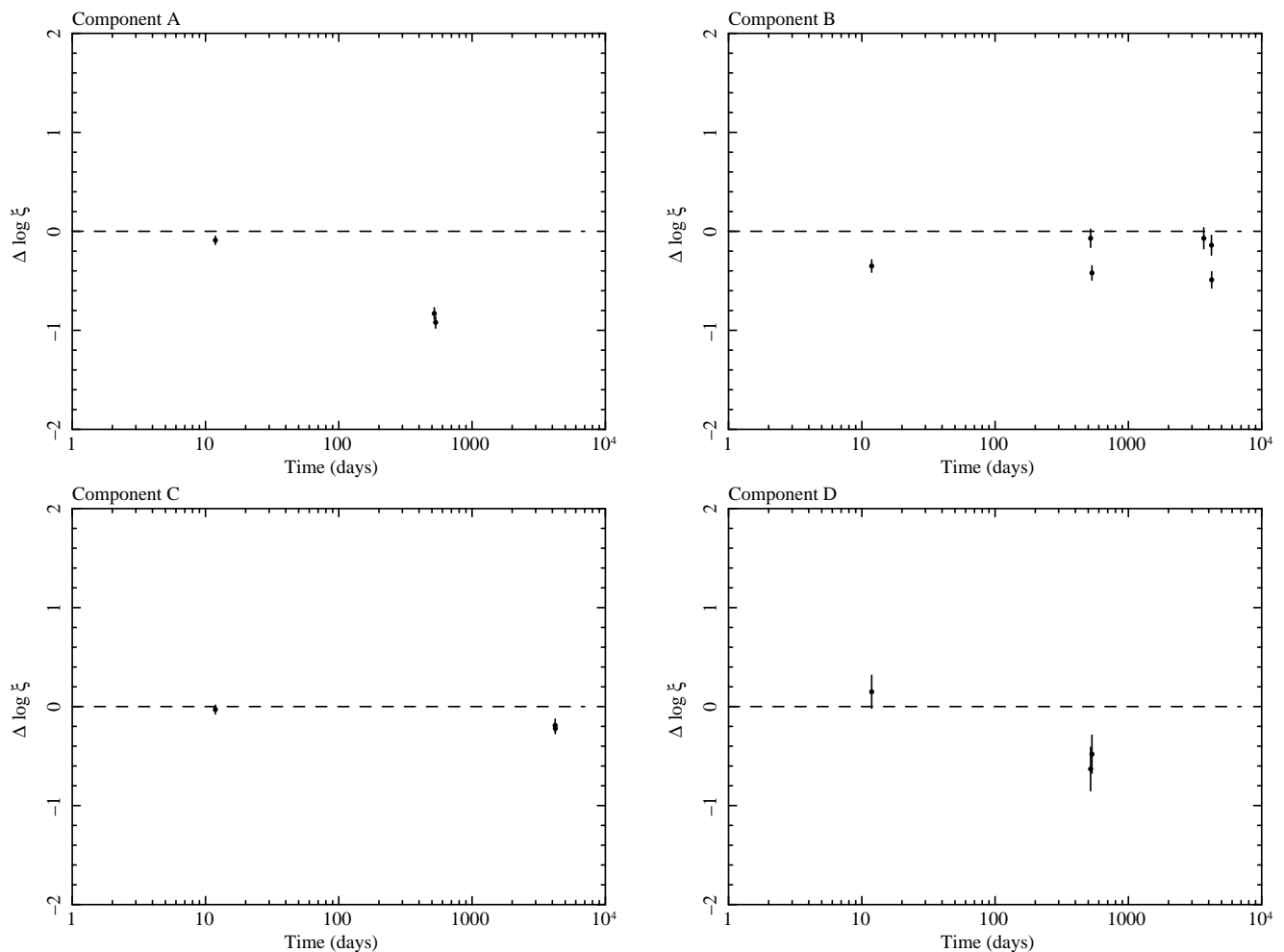


Fig. 5. Variation in the ionization parameter $\Delta \log \xi$ at different time scales (in days) for WA components *A* and *B* (top panels), and *C* and *D* (bottom panels).

With the average $\langle nt_{rec} \rangle$ for each component, and using the estimated time scales for variability (upper limits on t_{rec}) and nonvariability (lower limits on t_{rec}) described above, we can obtain lower and upper limits on the density of the absorbing gas, respectively, for each component. As expected, the component that changes the fastest is the one with the highest density, component *B*, with a density higher than $\log n = 4.8 \text{ cm}^{-3}$. The remaining components can have densities as high as $\log n \sim 4.9 \text{ cm}^{-3}$, based on their nonvariability. Among them, component *C* is possibly the less dense gas since it only shows variability on time scales of ~ 12 years. These values are shown in Table 6.

6.3. Location of the absorbers

From the definition of the ionization parameter in Eq. 1, the distance of the ionized gas to the central source is given by:

$$R = \sqrt{\frac{L_{ion}}{n\xi}}. \quad (4)$$

The ionizing luminosity of NGC 985 was calculated by integrating the obscured SED between 1 and 1000 Ryd for all observations and then averaging to obtain a value of $4.7 \times 10^{44} \text{ erg s}^{-1}$. This is the ionizing flux that is seen by the WA components after

being filtered by the obscurer. From Eq. 4 and using the upper and lower limits on the gas density derived in Sect. 6.2, we can obtain lower and upper limits on the distance at which the WA components lie. The results are summarized in Table 6.

The denser gas, faster to respond to flux changes, in component *B* is located at ~ 2 pc or less from the ionizing source. Since we did not probe variability (or lack of) at time scales smaller than 12 days, we cannot set a lower limit on its location. Component *A* is located between 1 to ~ 7 pc from the central SMBH. It is therefore unlikely that this WA component and the obscurer share the same *locus*, as discussed in Sect. 6.1. Component *C* responds at much longer time scales which would mean that the gas is less dense. For this component we derive the farthest upper limit on the distance, $\lesssim 60$ pc, although it can also be located as close as 3 pc from the source. Finally, component *D* is likely located between 5 and 30 pc.

To put these values into context we can use the relation in Kaspi et al. (2005) to estimate the location of the BLR in NGC 985. We obtain $R_{BLR} \sim 16$ light-days, or ~ 0.013 pc, so it is clear that all the WA components are outflowing much further away. The inner side of the putative dusty torus around the central engine can be approximated by the dust sublimation radius, which is $\sim L_{ion,44}^{1/2}$ pc (Krolik & Kriss 2001). For our measured L_{ion} , this value is ~ 2.5 pc. The picture that arises from these values is somewhat similar to what was seen in the stability curves (Fig. 4). Components *A* and *B* are possibly located at pc-scale

Table 6. Variability time scales, density, and location of the WA components in NGC 985.

Component	$\langle nt_{\text{rec}} \rangle$ (s cm ⁻³)	$t_{\text{rec}}^{\text{lower}}$ (days)	$t_{\text{rec}}^{\text{upper}}$ (days)	$\log n^{\text{lower}}$ (cm ⁻³)	$\log n^{\text{upper}}$ (cm ⁻³)	R^{lower} (pc)	R^{upper} (pc)
<i>A</i>	7.0×10^{10}	> 12	< 520	> 3.2	< 4.9	> 1	< 7
<i>B</i>	6.9×10^{10}	> 0	< 12	> 4.8	< 2
<i>C</i>	5.1×10^{10}	> 12	< 4200	> 2.2	< 4.7	> 3	< 60
<i>D</i>	4.9×10^{10}	> 12	< 520	> 3.0	< 4.7	> 5	< 30

distances, with *B* likely closer to the central SMBH but still far from the BLR. They have similar ionization states, but their kinematics are substantially different. Having ruled out that the much faster component *A* is related to the obscurer, it is possible that both components are powered by different acceleration mechanisms. On the other hand, components *C* and *D* may extend up to several tens of pc from the ionizing source. Their location and density are consistent with the typical values of the gas in the NLR of AGN (see e.g., Whewell et al. 2015), although their lower limits may bring them closer to the location of components *A* and *B*.

It is worth noting that, in principle, a similar approach to estimate the variability scale, the limits on the density, and ultimately the location could be followed also for the obscurer. However, the obscurer has additional constraints as it is clearly observed in the HST UV data. Given the line widths and covering fractions observed in the UV, the obscurer must be located within the BLR (Ebrero et al. 2016a; Kriss et al., in prep.). Constraining the location of the obscurer in X-rays by means of variability changes that provide results compatible with the UV observations would require a much shorter sampling (typically much less than a day). The available datasets, particularly the highly obscured ones in which the obscurer is almost fully covering our line of sight, lack the required signal-to-noise and exposure times to perform this kind of analysis reliably. Therefore in what follows, we rely on the constraints from the UV observations and assume that the obscurer is located within 16 light-days from the central ionizing source.

6.4. Energy budget of the absorbers

The distance constraints obtained in Section 6.3 allow us to estimate the amount of mass per unit time carried by the X-ray outflows in NGC 985. Assuming that the outflow moves away radially with constant speed v , in the form of a partial thin spherical shell at a distance R from the central source, the amount of mass per unit time carried in an outflow is given by:

$$\dot{M}_{\text{out}} = \mu m_p N_{\text{H}} v R \Omega, \quad (5)$$

where $\mu = 1.4$ is the mean atomic mass per proton, m_p is the proton mass, and Ω is the solid angle subtended by the outflow as seen from the central source, which ranges by definition between 0 and 4π sr. This parameter is usually unknown, as it depends on the actual geometry of the outflow although it is typically estimated to be $\pi/2$ sr, based on the observed type-1 to type-2 ratio in nearby Seyfert galaxies (Maiolino & Rieke 1995), plus the fact that warm absorbers are detected approximately in half the observed Seyfert 1 galaxies (Dunn et al. 2007). Indeed, this estimation for Ω is based on statistics that might be biased by selection effects (e.g., the fact that no warm absorber is detected in a given Seyfert galaxy might be due to the outflow geometry, but also to the lack of instrumental sensitivity).

From Eq. 5 it follows that the faster, more massive winds, will carry more mass into the ISM of the host galaxy. Similarly, the outflows located further away will carry more mass per unit time than those located much closer to the central source even if the latter are denser. This is clearly exemplified in Component *A* which has large column, fast speed, outflowing at pc-scale distances. Taking the upper limit on the distance for this component we obtain that this outflow has, at most, a mass rate of $\sim 6.5\Omega M_{\odot} \text{ yr}^{-1}$. This is the bulk of the mass outflow rate in this AGN, several times higher than those of components *B*, *C*, and *D*, with $\dot{M}_{\text{out}} \sim 0.5\Omega$, $\sim 1.2\Omega$, and $\sim 0.2\Omega M_{\odot} \text{ yr}^{-1}$, respectively. Even the obscurer, which has comparable column density and velocity, has a considerably less impact on its surroundings because it is significantly closer to the central SMBH, with an estimated \dot{M}_{out} of around $\sim 0.04\Omega M_{\odot} \text{ yr}^{-1}$, using as upper limit on its distance the 16 light-days at which the BLR is likely located based on the UV data.

The values of \dot{M}_{out} listed in Table 7 were obtained assuming that the solid angle subtended by the outflows is $\Omega = \pi/2$ sr, and must be considered upper limits, as they were calculated with the estimated upper limits on their distance. The total mass rate conveyed by the X-ray outflows is $\sim 13 M_{\odot} \text{ yr}^{-1}$, also an upper limit. For comparison, the SMBH in NGC 985 is accreting matter at a rate given by:

$$\dot{M}_{\text{acc}} = \frac{L_{\text{bol}}}{\eta c^2}, \quad (6)$$

where $\eta = 0.1$ is the nominal accretion efficiency, c is the speed of light, and L_{bol} is the bolometric luminosity of NGC 985. Integrating the unobscured SED we obtain $L_{\text{bol}} \sim 10^{46} \text{ erg s}^{-1}$, which translates into a mass accretion rate of $\dot{M}_{\text{acc}} = 1.76 M_{\odot} \text{ yr}^{-1}$. Therefore, the AGN in NGC 985 expels from its surroundings up to 7 times more matter than it actually accretes. This is a value often seen in Seyfert galaxies (Blustin et al. 2005; Ebrero et al. 2010, 2016b; see also Costantini 2010), but still an order of magnitude less than other extreme cases (Crenshaw & Kraemer 2012; Ebrero et al. 2013).

From the mass outflow rate is then trivial to obtain the kinetic luminosity of the outflows:

$$L_{\text{KE}} = \frac{1}{2} \dot{M}_{\text{out}} v^2. \quad (7)$$

It can be seen that the WA components in NGC 985 have L_{KE} values of $\sim 10^{41} \text{ erg s}^{-1}$, with the exception of component *A*, which is two orders of magnitude higher and is therefore the major contributor to the feedback in this AGN. Indeed, the kinetic luminosity of this WA component accounts for $\sim 0.8\%$ of the bolometric luminosity of the source. This would mean that this outflow by itself might be carrying enough mass and energy to significantly disrupt the ISM of NGC 985, as it is within the

Table 7. Energetics of the X-ray WA components. The solid angle subtended by the WA is assumed to be $\Omega = \pi/2$ sr.

Component	\dot{M}_{out}^a	$\dot{M}_{\text{out}}/\dot{M}_{\text{acc}}$	$\log L_{\text{KE}}^b$	$L_{\text{KE}}/L_{\text{bol}}$
<i>O</i>	0.07	0.04	41.9	0.008%
<i>A</i>	10.3	6.5	43.9	0.8%
<i>B</i>	0.9	0.5	41.1	0.001%
<i>C</i>	1.9	1.1	40.9	0.0008%
<i>D</i>	0.3	0.2	40.5	0.0003%
Total	13.47	8.34	43.93	0.81%

Notes. ^(a) Mass outflow rate, in units of $M_{\odot} \text{ yr}^{-1}$; ^(b) kinetic luminosity, in units of erg s^{-1} .

range 0.5% – 5% of the bolometric luminosity that is required by the models to be fed back into the medium to reproduce the observed $M - \sigma$ relation (see Hopkins & Elvis 2010, and references therein). This would then be one of the few cases in which a regular, moderate velocity warm absorber wind is deemed as a source of feedback.

It is to be emphasized that the presence of obscuring winds arising from very close to the accretion disk is possibly a more common phenomenon than originally thought as monitoring campaigns increase. This is important not only for the overall understanding of these transient events, but also for the effects on the photoionized gas that surrounds the central engine as the ionizing continuum dims and brightens again. Catching an AGN either entering or exiting an obscuration event is thus crucial to constrain the physical characteristics of the ionized gas around the central SMBH.

7. Conclusions

NGC 985 was observed twice by *XMM-Newton* in 2015 revealing that the source was coming out from a soft X-ray obscuration episode that took place in 2013 (Parker et al. 2014; Ebrero et al. 2016a). In this work we have analyzed the high-resolution X-ray spectra of these observations obtained by RGS together with another *XMM-Newton* archival observation in 2003, when the source was mildly obscured, possibly arising from another past obscuration event.

The complex absorption spectra of NGC 985 reveals the presence of four warm absorber (WA) outflows, with column densities ranging from $\sim 10^{21}$ to a few times 10^{22} cm^{-2} . The highest ionization component *A*, with $\log \xi \simeq 2.9$, is also the fastest ($v_{\text{out}} \sim -5100 \text{ km s}^{-1}$). Components *B* and *D*, with $\log \xi$ around 2.6 and 1.6, respectively, have similar kinematics ($\sim -600 \text{ km s}^{-1}$), while component *C* has $\log \xi = 2.0$ and is the slowest, outflowing at $\sim -350 \text{ km s}^{-1}$. The obscurer is characterized by a mildly ionized wind ($\log \xi \sim 0.2 - 0.5$) with $N_{\text{H}} \sim 2 \times 10^{22} \text{ cm}^{-2}$, moving away at a projected velocity of $\sim -6000 \text{ km s}^{-1}$.

The multi-epoch analysis of these WA components and the obscurer showed that their parameters changed throughout the different observations, when the ionizing flux varied as the obscuration event was taking place and then progressively faded away. Assuming that the gas is in equilibrium and that the changes are due to photoionization and recombination processes in response to changes in the ionizing flux, we estimated upper and lower limits on the gas density based on the various variability and nonvariability time scales probed by the observations. These limits can then be used in turn to put stringent constraints

on the location of the WA. These outflows are located at pc-scale distances (components *A* and *B*), compatible with the inner edge of the torus, or tens of pc (components *C* and *D*), similar to the NLR distance estimated in other AGN, from the central ionizing source. There is, however, no evidence of a connection between the emitting gas and the WA. The emission lines detected in the RGS spectra of NGC 985 are typically narrow and do not show any significant blueshift in their centroids. On the other hand, the obscurer is likely located much closer to the accretion disk, possibly close to the BLR based on the UV data.

In spite of the similar kinematics, columns and co-location on the stability curves, it is very unlikely that the obscurer and WA component *A* belong to the same long-lived structure. It cannot be ruled out that component *A* is actually an ejecta from the obscurer that has travelled further away until it has intersected our line of sight in the course of these observations. If we assume that it was launched close to the central engine, perhaps in the form of a disk wind, and that it has been traveling at the current measured velocity (i.e., that no other acceleration mechanism was in place), then the outflow has needed ~ 300 years to reach the lower limit on the location of component *A* (~ 2 pc). Considering all these assumptions and the long time scales involved it is unclear that there is a causal connection between these two components. On the other hand, the different limits derived on the distance for the WA, and their respective ionization parameters, may suggest that the WA is stratified, with the different components being launched from different parts of the disk.

In terms of mass and energy deposited back into the ISM of NGC 985, WA component *A* carries the bulk of the mass and the kinetic energy per unit time, owing to its distance to the AGN engine, density, and velocity. This component by itself could carry enough momentum to disturb the ISM, as its kinetic luminosity is about 0.8% of the bolometric luminosity of the AGN. This value is within the range of $L_{\text{KE}}/L_{\text{bol}}$ fraction required by many models to account for cosmic feedback.

Observations of the onset and the ending of transient eclipsing events in AGN is therefore a key opportunity to study the obscuring matter itself, but also the impact on the surrounding gas as the ionizing flux varies.

Acknowledgements. This work is based on observations obtained by *XMM-Newton*, an ESA science mission with instruments and contributions directly funded by ESA member states and the USA (NASA). V.D. acknowledges support from the ESA Trainee program and the ESAC Space Science Faculty. This work was supported by NASA through a grant for HST program number 13812 from the Space Telescope Science Institute, which is operated by the Association of Universities for Research in Astronomy, Incorporated, under NASA contract NAS5-26555. SRON is supported financially by NWO, the Netherlands Organization for Scientific Research.

References

- Arav, N. 2002, in X-ray Spectroscopy of AGN with Chandra and XMM-Newton, ed. T. Boller, S. Komossa, S. Kahn, H. Kunieda, & L. Gallo, 153
- Blustin, A. J., Page, M. J., Fuerst, S. V., Branduardi-Raymont, G., & Ashton, C. E. 2005, *A&A*, 431, 111
- Bottoff, M. C., Korista, K. T., & Shlosman, I. 2000, *ApJ*, 537, 134
- Cardelli, J. A., Clayton, G. C., & Mathis, J. S. 1989, *ApJ*, 345, 245
- Cash, W. 1979, *ApJ*, 228, 939
- Costantini, E. 2010, *Space Sci. Rev.*, 157, 265
- Crenshaw, D. M. & Kraemer, S. B. 2012, *ApJ*, 753, 75
- Crenshaw, D. M., Kraemer, S. B., & George, I. M. 2003, *ARA&A*, 41, 117
- den Herder, J. W., Brinkman, A. C., Kahn, S. M., et al. 2001, *A&A*, 365, L7
- Di Gesu, L., Costantini, E., Ebrero, J., et al. 2015, *A&A*, 579, A42
- Di Matteo, T., Springel, V., & Hernquist, L. 2005, *Nature*, 433, 604
- Dunn, J. P., Crenshaw, D. M., Kraemer, S. B., & Gabel, J. R. 2007, *AJ*, 134, 1061

- Ebrero, J., Costantini, E., Kaastra, J. S., et al. 2010, *A&A*, 520, A36
- Ebrero, J., Kaastra, J. S., Kriss, G. A., de Vries, C. P., & Costantini, E. 2013, *MNRAS*, 435, 3028
- Ebrero, J., Kaastra, J. S., Kriss, G. A., et al. 2016b, *A&A*, 587, A129
- Ebrero, J., Kriss, G. A., Kaastra, J. S., & Ely, J. C. 2016a, *A&A*, 586, A72
- Ferland, G. J., Porter, R. L., van Hoof, P. A. M., et al. 2013, *Rev. Mexicana Astron. Astrofis.*, 49, 137
- Fisher, K. B., Huchra, J. P., Strauss, M. A., et al. 1995, *ApJS*, 100, 69
- Fukumura, K., Kazanas, D., Contopoulos, I., & Behar, E. 2010a, *ApJ*, 715, 636
- Fukumura, K., Kazanas, D., Contopoulos, I., & Behar, E. 2010b, *ApJ*, 723, L228
- Gabriel, C., Denby, M., Fyfe, D. J., et al. 2004, in *Astronomical Society of the Pacific Conference Series*, Vol. 314, *Astronomical Data Analysis Software and Systems (ADASS) XIII*, ed. F. Ochsenbein, M. G. Allen, & D. Egret, 759
- George, I. M., Turner, T. J., Netzer, H., et al. 1998, *ApJS*, 114, 73
- Hopkins, P. F. & Elvis, M. 2010, *MNRAS*, 401, 7
- Kaastra, J. S. & Barr, P. 1989, *A&A*, 226, 59
- Kaastra, J. S., Kriss, G. A., Cappi, M., et al. 2014, *Science*, 345, 64
- Kaastra, J. S., Mewe, R., Liedahl, D. A., Komossa, S., & Brinkman, A. C. 2000, *A&A*, 354, L83
- Kaastra, J. S., Mewe, R., & Nieuwenhuijzen, H. 1996, in *UV and X-ray Spectroscopy of Astrophysical and Laboratory Plasmas*, ed. K. Yamashita & T. Watanabe, 411–414
- Kalberla, P. M. W., Burton, W. B., Hartmann, D., et al. 2005, *A&A*, 440, 775
- Kaspi, S., Brandt, W. N., Netzer, H., et al. 2001, *ApJ*, 554, 216
- Kaspi, S., Maoz, D., Netzer, H., et al. 2005, *ApJ*, 629, 61
- Kim, M., Ho, L. C., Peng, C. Y., et al. 2008, *ApJ*, 687, 767
- Kinney, A. L., Calzetti, D., Bohlin, R. C., et al. 1996, *ApJ*, 467, 38
- Königl, A. & Kartje, J. F. 1994, *ApJ*, 434, 446
- Krolik, J. H. & Kriss, G. A. 2001, *ApJ*, 561, 684
- Krolik, J. H., McKee, C. F., & Tarter, C. B. 1981, *ApJ*, 249, 422
- Krongold, Y., Jiménez-Bailón, E., Santos-Lleo, M., et al. 2009, *ApJ*, 690, 773
- Krongold, Y., Nicastro, F., Elvis, M., et al. 2005, *ApJ*, 620, 165
- Laha, S., Guainazzi, M., Chakraborty, S., Dewangan, G. C., & Kembhavi, A. K. 2016, *MNRAS*, 457, 3896
- Lodders, K. & Palme, H. 2009, *Meteoritics and Planetary Science Supplement*, 72, 5154
- Longinotti, A. L., Kriss, G., Krongold, Y., et al. 2019, *ApJ*, 875, 150
- Longinotti, A. L., Krongold, Y., Kriss, G. A., et al. 2013, *ApJ*, 766, 104
- Maiolino, R. & Rieke, G. H. 1995, *ApJ*, 454, 95
- Mehdipour, M., Kaastra, J. S., Kriss, G. A., et al. 2017, *A&A*, 607, A28
- Mehdipour, M., Kaastra, J. S., Kriss, G. A., et al. 2016, *A&A*, 588, A139
- Mehdipour, M., Kaastra, J. S., Kriss, G. A., et al. 2015, *A&A*, 575, A22
- O'Donnell, J. E. 1994, *ApJ*, 422, 158
- Parker, M. L., Schartel, N., Komossa, S., et al. 2014, *MNRAS*, 445, 1039
- Porquet, D. & Dubau, J. 2000, *A&AS*, 143, 495
- Proga, D. & Kallman, T. R. 2004, *ApJ*, 616, 688
- Rees, M. J. 1984, *ARA&A*, 22, 471
- Reynolds, C. S. 1997, *MNRAS*, 286, 513
- Risaliti, G., Elvis, M., Fabbiano, G., et al. 2007, *ApJ*, 659, L111
- Risaliti, G., Nardini, E., Salvati, M., et al. 2011, *MNRAS*, 410, 1027
- Schlafly, E. F. & Finkbeiner, D. P. 2011, *ApJ*, 737, 103
- Schlegel, D. J., Finkbeiner, D. P., & Davis, M. 1998, *ApJ*, 500, 525
- Tombesi, F., Cappi, M., Reeves, J. N., & Braito, V. 2012, *MNRAS*, 422, L1
- Tombesi, F., Cappi, M., Reeves, J. N., et al. 2013, *MNRAS*, 430, 1102
- Whewell, M., Branduardi-Raymont, G., Kaastra, J. S., et al. 2015, *A&A*, 581, A79

Appendix A: XMM-Newton RGS spectra of NGC 985

In this Appendix section we show the RGS spectra used in this work together with their best-fit model. The 2003 observation is shown in Fig. A.1, the 2013 observation in Fig. A.2, and the first observation of 2015 in Fig. A.3.

Appendix B: Plots of the absorption models

In this Appendix section we show the model plots of the different absorption components detected in the XMM-Newton observations. In this way we show the contribution in different parts of the spectra of the different components. The different absorption components have been shifted in flux for clarity.

Appendix C: Ionic species used for variability calculations

In Tables C.1 to C.4 we list the ions that were used in Sect. 6.2 as a proxy for each WA component, and their corresponding product nt_{rec} as provided by the SPEX auxiliary program *rec_time*.

Table C.1. Ions used as a proxy for the WA component A.

Ion	nt_{rec} (s cm ⁻³)
Na XI	7.6×10^{10}
Mg XII	1.2×10^{11}
Fe XX	3.1×10^{10}
Fe XXIV	5.4×10^{10}

Table C.2. Ions used as a proxy for the WA component B.

Ion	nt_{rec} (s cm ⁻³)
N VII	1.6×10^{10}
O VIII	3.0×10^{10}
Ne X	8.8×10^{10}
Na XI	1.7×10^{11}
Mg XI	6.2×10^{10}
Mg XII	8.0×10^{10}
Si XIII	1.8×10^{11}
Fe XVIII	2.3×10^{10}
Fe XIX	2.2×10^{10}
Fe XX	1.4×10^{10}

Table C.3. Ions used as a proxy for the WA component C.

Ion	nt_{rec} (s cm ⁻³)
C VI	3.0×10^{10}
N VI	1.4×10^{11}
N VII	7.7×10^{10}
O VII	2.4×10^{10}
O VIII	1.1×10^{11}
Ne IX	1.4×10^{11}
Ne X	1.1×10^{11}
Mg XI	5.2×10^{10}
Ar XI	2.5×10^{10}
Ar XII	9.6×10^{10}
Ar XIII	3.8×10^{10}
Ca XIII	5.0×10^{10}
Fe X	2.8×10^9
Fe XI	3.2×10^9
Fe XII	2.6×10^{10}
Fe XIII	4.7×10^9

Table C.4. Ions used as a proxy for the WA component D.

Ion	nt_{rec} (s cm ⁻³)
C VI	1.0×10^{11}
N VI	5.5×10^{10}
O VII	9.5×10^{10}
Ar XI	6.0×10^{10}
Fe VIII	2.7×10^{10}
Fe IX	2.1×10^9
Fe X	3.8×10^{11}

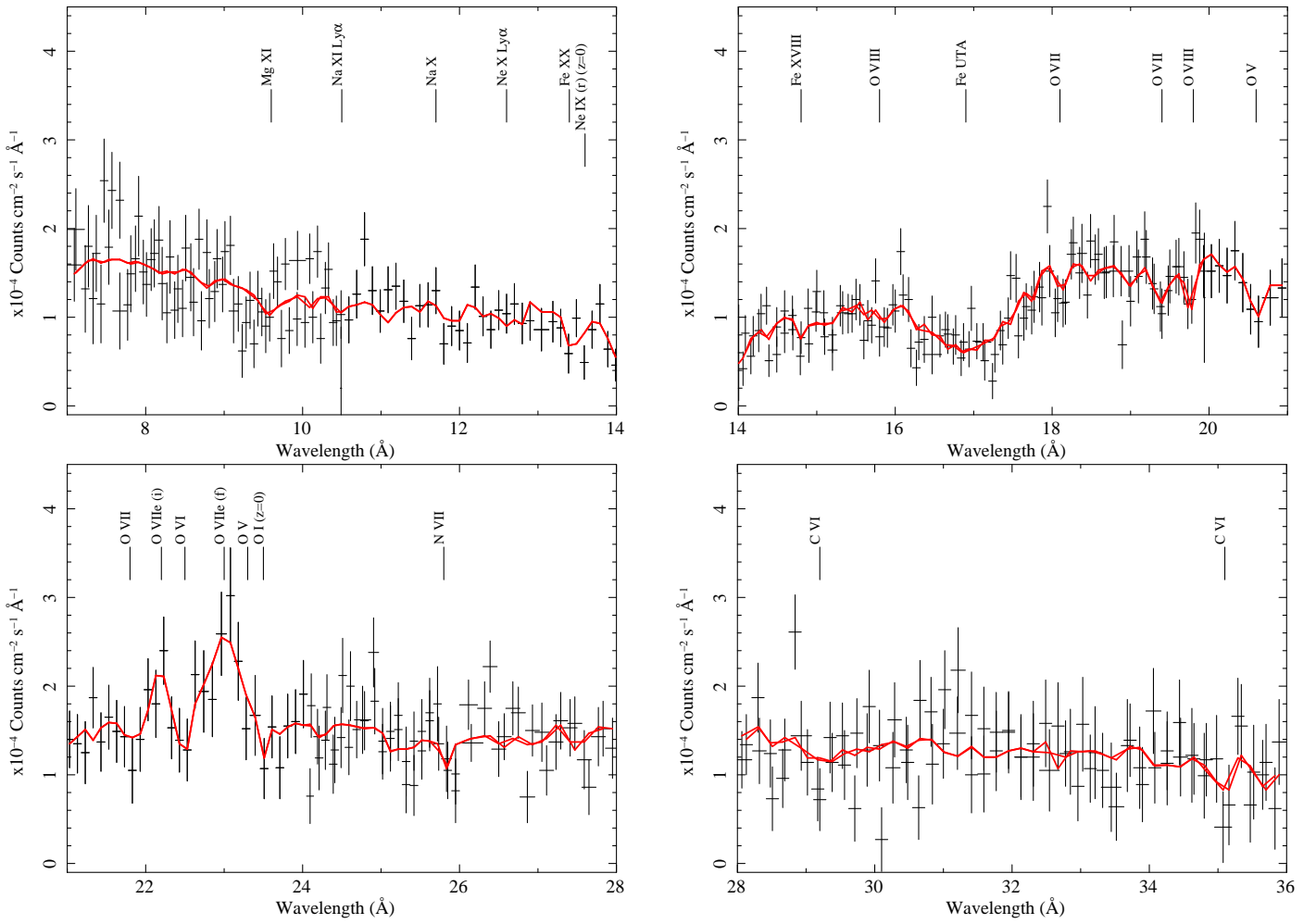


Fig. A.1. XMM-Newton RGS spectrum of NGC 985 in 2003. The solid red line represents the best fit model. The most relevant features have been labeled.

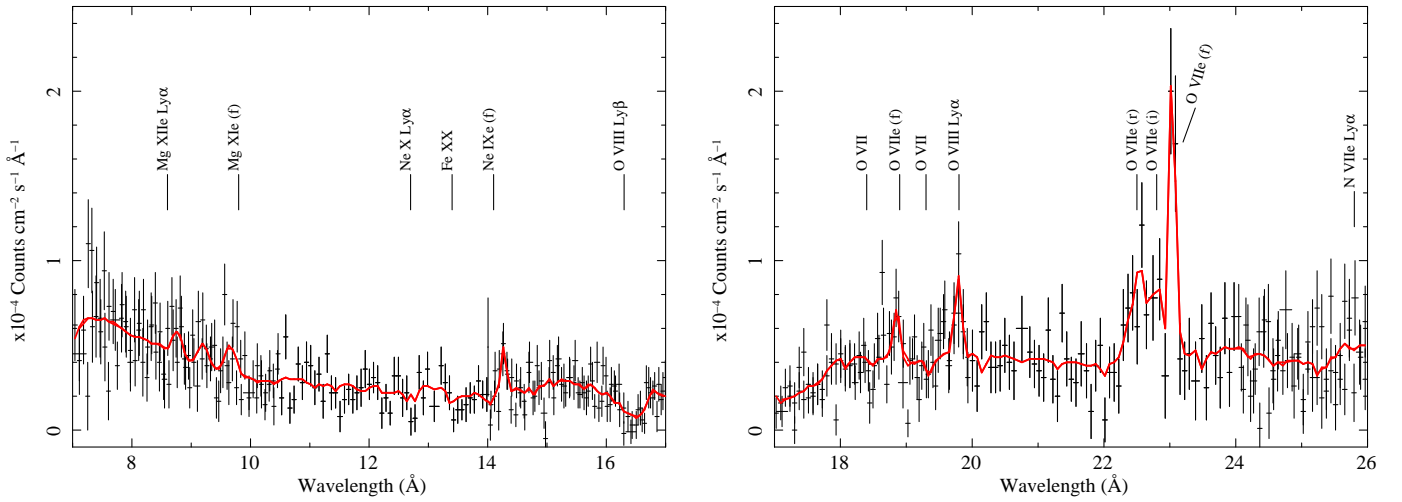


Fig. A.2. XMM-Newton RGS spectrum of NGC 985 in 2013. The solid red line represents the best fit model. The spectrum has been rebinned for clarity. The most relevant features have been labeled.

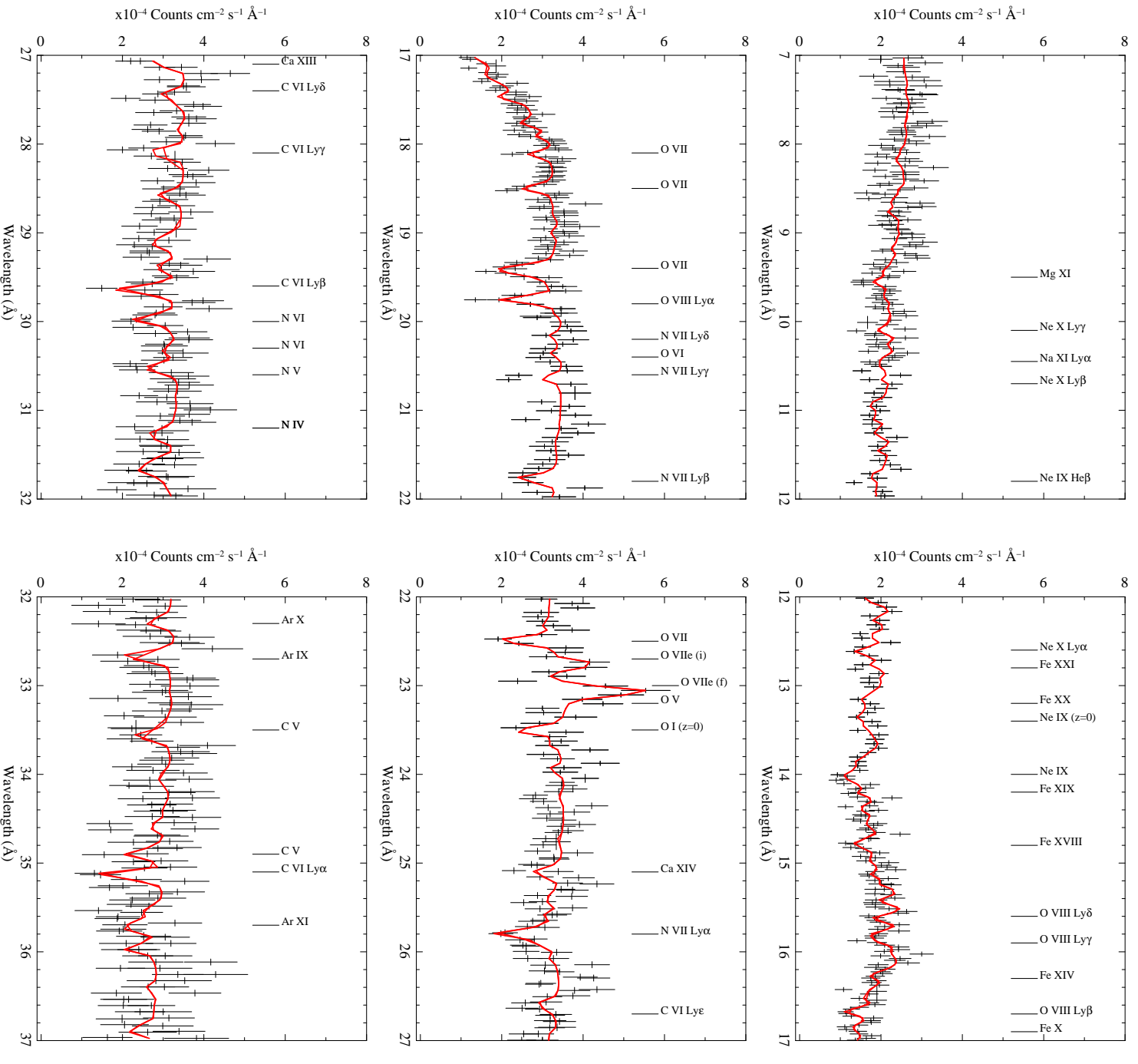


Fig. A.3. XMM-Newton RGS spectrum of NGC 985 in 2015 (first observation). The solid red line represents the best fit model. The most relevant features have been labeled.

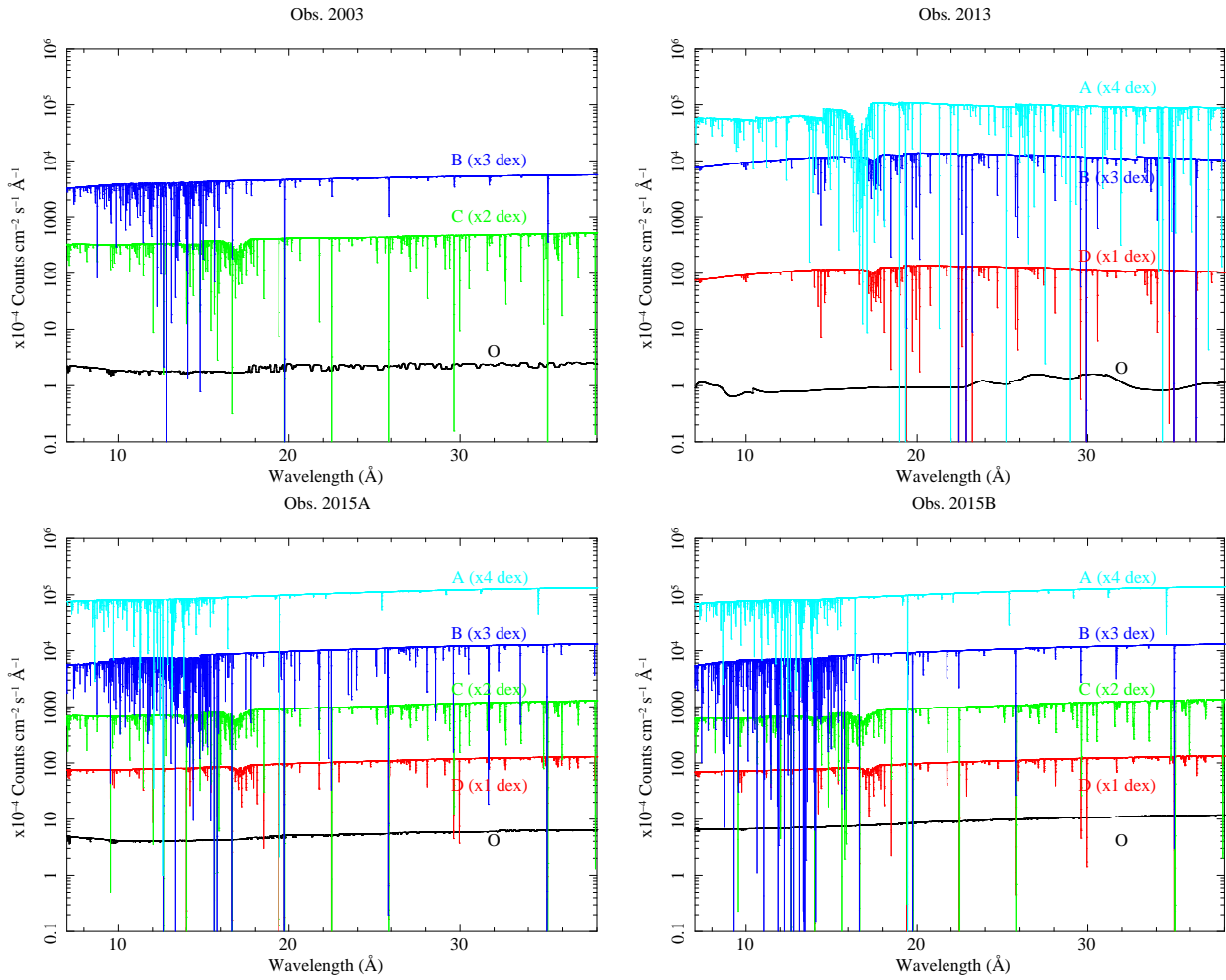


Fig. B.1. Model plot showing the contribution to the RGS spectrum of each of the *xabs* components that model the absorption troughs seen in NGC 985 for the observations in 2003 (*upper left panel*), 2013 (*upper right panel*), 2015a (*lower left panel*), and 2015b (*lower right panel*). For clarity, the contribution of Component *D* has been shifted by 1 dex in flux, the one of Component *C* by 2 dex, the one of Component *B* by 3 dex, and the one of Component *A* by 4 dex, whenever they have been detected.